



Tac-scope: An endoscope integrated with soft sensor for real-time tactile feedback

Yingxuan Zhang, Qi Jiang*, Feiwen Wang, Jie Wang, Maosheng Ye, Dongxuan Li

Shandong University, Jingshi Road #17923, Jinan, 250061, China

ARTICLE INFO

Keywords:

Endoscope
Tactile sensor
Force detection
Orientation detection
Tactile-vision feedback

ABSTRACT

In order to improve the safety of endoscopic surgery, a flexible endoscope with real-time tactile feedback (Tac-scope) has been proposed. It integrates a soft sensor at the end embedded with fiber Bragg grating (FBG) to detect the contact force with the lumen wall, while retaining the original function of the endoscope. In this article, theoretical analysis, simulated analysis, and experiments have been implemented, obtaining the mapping from FBG wavelength shifts to the force magnitude and orientation. To verify the real-time detection and feedback capability, tests are conducted on the bronchial model. The results show an average reduction of 60% in contact force and 30% in operation time. The linearity of Tac-scope force detection is 0.991, the repeatability error is 6.46%, the resolution is 8.8 mN, the sensitivity is 0.693 nm/N, the average error is 4.4%, and the error of orientation detection is 3.57%. Such merits indicate that the proposed Tac-scope has huge potential in endoscopic surgeries.

1. Introduction

Tactile feedback plays an important role in ensuring the safety and maneuverability of natural orifice transluminal endoscopic surgery (NOTES) [1,2]. It can significantly reduce the risk of abrasions caused by collisions between the endoscope and the inner wall of the lumen due to the lack of visual depth information or unclear images [3,4]. Robot-assisted surgery (RAS) can reduce contact caused by flutter. However, the lack of tactile feedback during endoscopic biopsy makes it difficult for the surgeon to judge the degree and orientation of the contact with the lumen. This makes it challenging to control the instrument in a timely manner.

Tactile feedback relies on tactile sensing, which is divided into indirect and direct sensing. The former is to calculate the contact force through posture and shape detection [5], or modeling estimation [6] of the flexible instrument. However, the complexity of the intraoperative environment may affect the accuracy of calculation. Direct sensing, which is more suitable for complex and dynamic environments detection, is to detect by integrating proximal or distal (end of the instrument) tactile sensor. However, the proximal sensors pose a challenge in obtaining accurate distal forces due to its location outside the human body [7–10], and factors such as transmission, tissue friction, and the variety of flexible manipulator arms [11] further complicate the process.

Touch/force sensors integrated at the end of surgical instruments are the focus of interest. The ability to interact directly with tissues intraoperatively makes the detection results more reliable. Sušić et al. [12] propose an encapsulated force-sensing device, which integrates a compact force sensor and a camera on its tip for articulated robotic endoscope palpation. Its rigid structure limits the application in flexible endoscopes. Several studies, including Nagatomo et al. [13], Shaikh et al. [14], and Zhang et al. [15], have proposed sensors for tissue surfaces palpation which can obtain force and stiffness. Additionally, Naidu et al. [16] and Kim et al. [17] propose tactile sensors integrated on the end of instruments for palpation and force feedback in minimally invasive surgeries. However, due to size constraints, it is challenging to integrate these devices with endoscope without compromising its function. In the study of Jin et al. [18], contact sensing with blood vessel is achieved by placing pressure-sensitive force sensor on the outside of the end of interventional catheter. This approach retains the original catheter structure, resulting in significant cost savings, but increases the catheter's outer diameter, making it difficult to access finer vessels. Ankur R. et al. [19] propose a sensor at the endoscope tip to decode contact force based on the interaction between the solenoid and the permanent magnet, providing contact force feedback for tracheal intubation. However, its application is limited to virtual training. Advances in new materials offer new ideas for sensing [20–22]. X. Guo

* Corresponding author.

E-mail addresses: zhangyingxuan@mail.sdu.edu.cn (Y. Zhang), jiangqi@sdu.edu.cn (Q. Jiang), wangfeiwen@mail.sdu.edu.cn (F. Wang), 202120628@mail.sdu.edu.cn (J. Wang), 202320776@mail.sdu.edu.cn (M. Ye), 202320772@mail.sdu.edu.cn (D. Li).

et al. propose a bamboo-inspired capacitive flexible sensor, which has high sensitivity and low cost [20]. It can be applied to health monitoring and human-computer interaction. However, medical endoscopes are compact, and flexible e-skin materials are not easy to integrate. FBG fibers are widely used for force sensing on surgical instruments due to their small size (diameter only 0.125 mm), flexibility, and passivity [23]. Several studies, including Zhang T et al. [24], Lai W et al. [25], and Du C et al. [26], have proposed FBG-based force sensors integrated on surgical instruments for puncture force, clamp force, and wrist force sensing. Additionally, Ping Z et al. [27] propose a miniaturized flexible instrument with FBG-based triaxial force sensing for intraoperative gastric endomicroscopy. Whereas, the use of a separate force detection tool may occupy the tool channel or add additional detection steps.

Thus, in this study, a flexible endoscope with an embedded FBG soft sensor (Tac-scope) has been proposed for contact sensing with the lumen wall. It allows for force value and orientation sensing, as well as soft contact. Real-time tactile feedback can be achieved while retaining the original function of the endoscope. Section 2 presents the structural design, theoretical analysis and simulated analysis. Section 3 gives the fabrication, calibration, compensation and validation of Tac-scope, and gives the test on bronchial model and the test of tactile-visual feedback.

2. Materials and methods

Due to the bronchus are narrower and more complex than other luminal environments and have more fragile tissues, it is used as the object for analysis in this paper.

2.1. Requirements analysis

In robot-assisted endoscopic surgery (RAES), the endoscope will contact the tracheal wall during its entrance. The contact force is usually about 1 N [28]. The force can be divided into normal force F_n and tangential force F_t (mainly friction force) [29]. Due to the complex shape of branches, as well as the long length of the bronchoscope in-depth, forces are complex and related to the number of contact points, as shown in Fig. 1. The endoscope will also be subjected to friction from the external delivery mechanism. The resulting force F can be expressed as:

$$F = \sum_{p=1}^y F_c(p) + F_{ex}(p). \quad (1)$$

$$F_c = F_n + F_t. \quad (2)$$

where F_c denotes the endoscope contact force to bronchial lumen, p denotes the label of contact point, y denotes the number of points, F_{ex} denotes the external frictional force from the delivery mechanism, $F_t = \mu F_n$, $\mu < 0.3$ [30]. The force of the airflow generated by breathing is ignored.

Of the many points of contact, the endoscope end with the inner wall is the most critical. The end plays a role in guiding the direction of the endoscope and preventing collisions. When the force is larger than the bronchial tube's tolerance range, the inner wall has the risk of bleeding. In order to improve the safety of RAES, the sensing and feedback of the end contact force is especially important. Due to the importance and the limited space of this paper, only end contact perception will be discussed.

2.2. Structural design

From the clinical needs, a novel flexible endoscope integrating a soft FBG tactile sensor at the end is proposed for detecting the contact force value and orientation, as shown in Fig. 2(b). The diameter of the Tac-scope is only 6 mm, allowing integration of lens and lights, and passage of biopsy tools, as shown in Fig. 2(c).

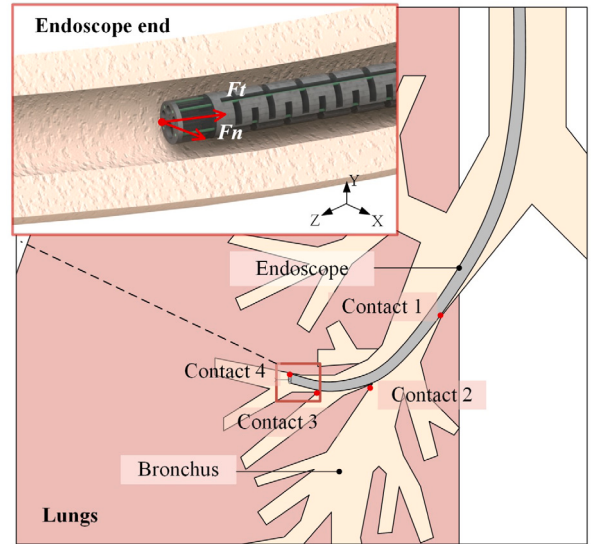


Fig. 1. Overlook of the Tac-scope in lungs.

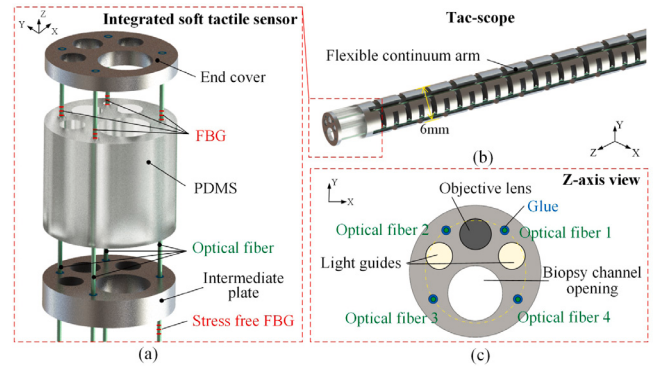


Fig. 2. (a) The structure of the integrated sensor (b) Overview of the Tac-scope (c) Z-axis view of the Tac-scope.

As shown in Fig. 2(a), The sensor is composed of three layers: the end cover, the polydimethylsiloxane (PDMS) soft layer, and the intermediate plate. The middle layer allows for soft contact with the lumen lining, which improves safety. The force-sensing elements are four fibers with FBG suspended in the soft layer. There is a stress-free FBG, which is 1 cm away from the suspended FBG for temperature compensation. In order to retain the lens and tool channels and to prevent the fiber channel from interfering with other, the optical fiber is arranged in a non-totally symmetric arrangement. In addition, optical fibers are suspended in the soft layer rather than embedded in it to lower the friction. There are four holes larger than the outer diameter of the fiber in the soft layer, and fibers are stuck and hung between the end cover and the intermediate plate.

2.3. Detection principle of the sensor

When the broad-band light is applied to the FBG, the grating transmits light of any wavelength but one. This wavelength is reflected [17], which is called the Bragg wavelength. Parameters such as strain and temperature are sensitive to the FBG, which will cause a shift in the Bragg wavelength [14]. It is given as:

$$\frac{\Delta\lambda_i}{\lambda_i} = \epsilon_i \{1 - 0.5n_{eff}^2 [p_{12} - v(p_{11} + p_{12})]\} + \zeta 4T. \quad (3)$$

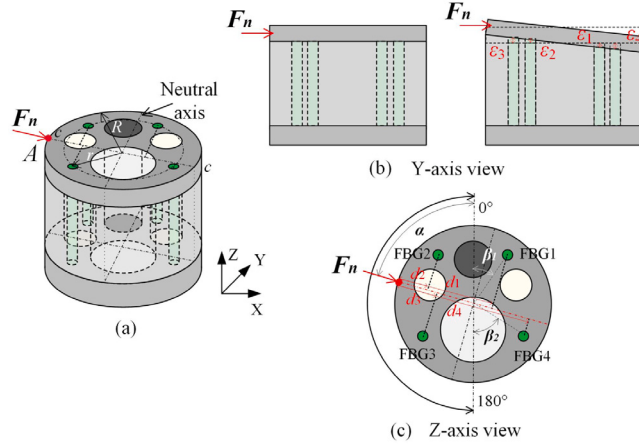


Fig. 3. The sensor under a force at orientation A (a) Overview (b) Y-axis view (c) Z-axis view.

where $\Delta\lambda_i$ denotes the wavelength shift of the FBG i ($i=1, 2, 3, 4$), λ_i denotes the initial central wavelength, ϵ_i denotes the axial fiber strain, n_{eff} denotes the effective refractive index, ν denotes the Poisson's ratio, p_{12} and p_{11} denote the strain-optical coefficients, ζ denotes the thermal-optical coefficient, and ΔT denotes the change of temperature.

To avoid getting affected by temperature during stress detection, an additional FBG is used to compensate [31]. The compensated stress is:

$$F_n \propto (\Delta\lambda_i - t\Delta\lambda_t). \quad (4)$$

where t is the temperature sensitivity coefficient, and $\Delta\lambda_t$ is the wavelength shift of the stress-free FBG.

During the endoscopic surgery, the endoscope contacts with the inner wall of the lumen with the force shown in Fig. 3(a). The force can be converted into axial strain of fibers, which will be stretched or compressed, as shown in Fig. 3(b). The strain ϵ_i can be given as:

$$\epsilon_i \propto \frac{h}{K_m} F_{ni} = a \frac{hd_i}{K_m} F_n. \quad (5)$$

where F_{ni} is the effective part of force F_n at FBG i , h and K_m are the thickness and hardness matrix of the soft layer, d_i is the radial length between FBG i and the orientation, and a is a constant value of the material.

It can be seen that when the contact orientation is a fixed value, the wavelength shift is related to F_n , h and K_m . If the these parameters are fixed, the wavelength shift is linearly related to F_n . It is obtained through optimization that the sensitivity and stability are higher when $h=5$ mm, and the sensitivity in detection range is higher when $K_m=30$ HA [32,33].

Strain is related not only to the magnitude of the contact force but also to the orientation. As shown in Fig. 3(c), the distances of the FBG projections on the transversal $c-c$ normal to the neutral axis and A are denoted as d_1, d_2, d_3, d_4 , respectively. With fixed force, the strains ϵ_i have a positive correlation with the length $2R - d_i$.

As the orientation A is changed from 0° to 180° , the relation between d_i and A (shown by the angle α) becomes:

$$\begin{aligned} d_1 &= R - r \cdot \cos(\beta_1 + \alpha) \\ d_2 &= R - r \cdot \cos(\beta_1 - \alpha) \\ d_3 &= R + r \cdot \cos(\beta_2 + \alpha) \\ d_4 &= R + r \cdot \cos(\beta_2 - \alpha) \end{aligned} \quad (6)$$

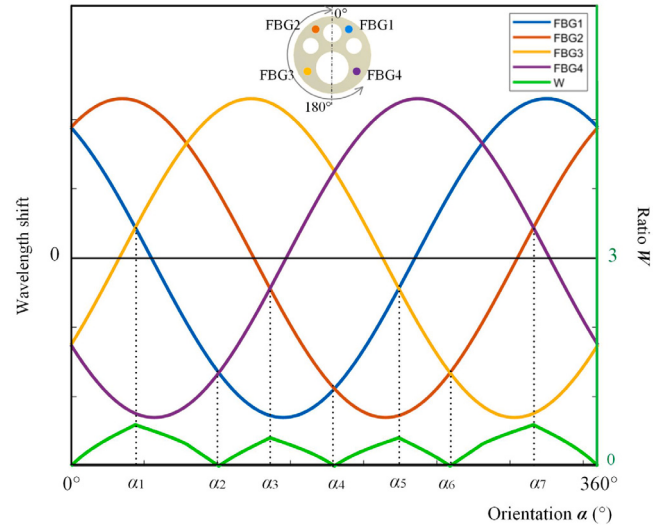


Fig. 4. The relationship between orientation and wavelength shifts.

Substituting Eq. (6) into (5) and (3):

$$\begin{aligned} \Delta\lambda_1 &= b[R + r \cdot \cos(\beta_1 + \alpha)]F_n \\ \Delta\lambda_2 &= b[R + r \cdot \cos(\beta_1 - \alpha)]F_n \\ \Delta\lambda_3 &= b[R - r \cdot \cos(\beta_2 + \alpha)]F_n \\ \Delta\lambda_4 &= b[R - r \cdot \cos(\beta_2 - \alpha)]F_n \end{aligned} \quad (7)$$

where λ is the initial central wavelength of four FBGs, and $b = a\lambda\{1 - 0.5n_{eff}^2[p_{12} - \nu(p_{11} + p_{12})]\}/K_m$ is invariant.

If F_n is fixed, the relation between FBG wavelength shifts and α is as shown in Fig. 4. It is shown that the wavelength shifts of the two FBGs closer to force orientation are smaller. The range of α can be estimated by comparing the magnitude of each wavelength shift. The ratio of the difference between them varies linearly with α , which is defined as W :

$$W = \begin{cases} C_1\alpha & 0^\circ \leq \alpha < \alpha 1 \\ C_1(\alpha 2 - \alpha 1)^{-1} + C_1\alpha & \alpha 1 \leq \alpha < \alpha 2 \\ C_2\alpha & \alpha 2 \leq \alpha < \alpha 3 \\ C_2(\alpha 4 - \alpha 3)^{-1} + C_2\alpha & \alpha 3 \leq \alpha < \alpha 4 \\ C_3\alpha & \alpha 4 \leq \alpha < \alpha 5 \\ C_3(\alpha 6 - \alpha 5)^{-1} + C_3\alpha & \alpha 5 \leq \alpha < \alpha 6 \\ C_4\alpha & \alpha 6 \leq \alpha < \alpha 7 \\ C_4(\alpha 8 - \alpha 7)^{-1} + C_4\alpha & \alpha 7 \leq \alpha < 360^\circ \end{cases} \quad (8)$$

where $C_1 = 0.5(1 + \Delta\lambda_j \Delta\lambda_g^{-1})$, $C_2 = 0.5(1 + \Delta\lambda_i \Delta\lambda_j^{-1})$, $C_3 = 0.5(1 + \Delta\lambda_j \Delta\lambda_i^{-1})$, $C_4 = 0.5(1 - \Delta\lambda_g \Delta\lambda_j^{-1})$.

From Eqs. (7) and (5), it can be seen that the slopes of force-strain are diverse at different orientations. Since the slope is constant, W does not change with the force. Values of coefficients C_1, C_2, C_3, C_4 can be obtained by calibration, then the α can be calculated. According to Eq. (5), the magnitude of F_n can be obtained by the wavelength shifts of any two FBGs:

$$F_n = \frac{\Delta\lambda_i - \Delta\lambda_j}{rb[\cos(\beta_2 + \alpha) - \cos(\beta_2 - \alpha)]}, (i = 3, j = 4) \quad (9)$$

2.4. Simulated analysis

The finite element (FE) model is established, the setup is shown in Fig. 5(a). The lower surface of the intermediate plate is fixed. To prevent buckling under stress, fibers are pre-tensioned with the force

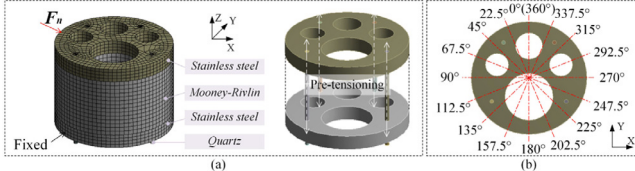


Fig. 5. (a) Setup of FE analysis (b) Orientations of the applied force.

Table 1
Material and parameters settings in the FE simulation.

Part of sensor	Material	Size	Young's modulus
End cover	Stainless steel	$\phi 6 \times 1.2$ mm	2×10^5 MPa
Middle soft layer	Mooney-Rivlin [34]	$\phi 6 \times 5$ mm	1.2 MPa
Intermediate plate	Stainless steel	$\phi 6 \times 1.2$ mm	2×10^5 MPa
Optical fibers	Quartz	$\phi 0.25$ mm	7.2×10^4 MPa

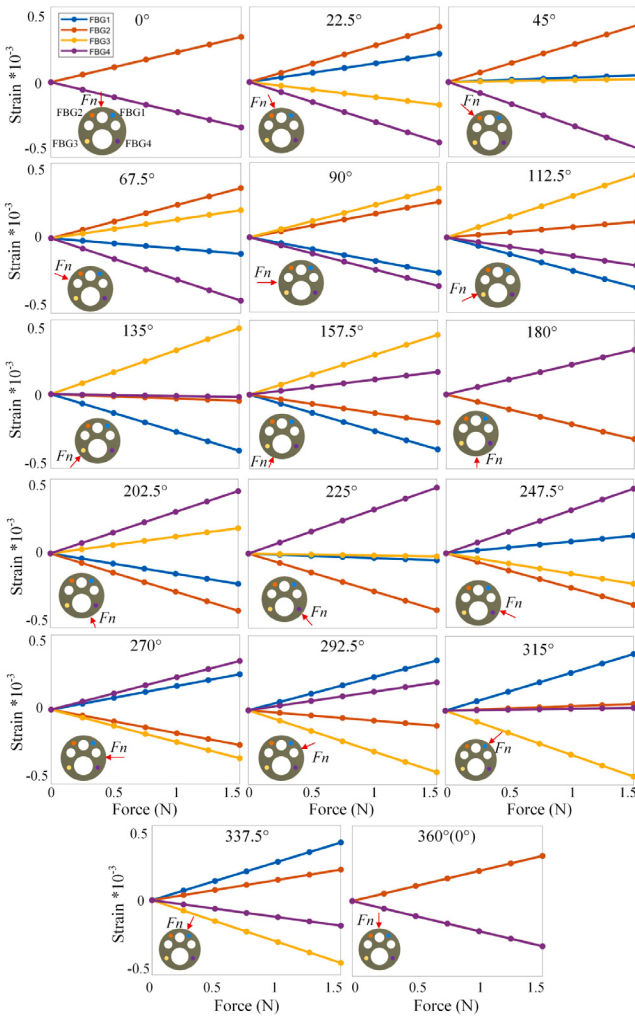


Fig. 6. The relationship between force and strain (simulation result).

of 1 N. The material and parameters settings are listed in **Table 1**. The F_n from 0 N to 1.5 N is successively applied at intervals of 0.25 N. The force will be transferred to the suspended fibers, resulting in wavelength shift of FBG, which is proportional to the strain. The orientations of force are shown in **Fig. 5(b)**, and they are taken at intervals of 22.5°. F_n is applied in the range of [0°, 360°].

The simulation result is shown in **Fig. 6**. It is clear that with the fixed orientation, the strain is linear with the force. When a force is applied

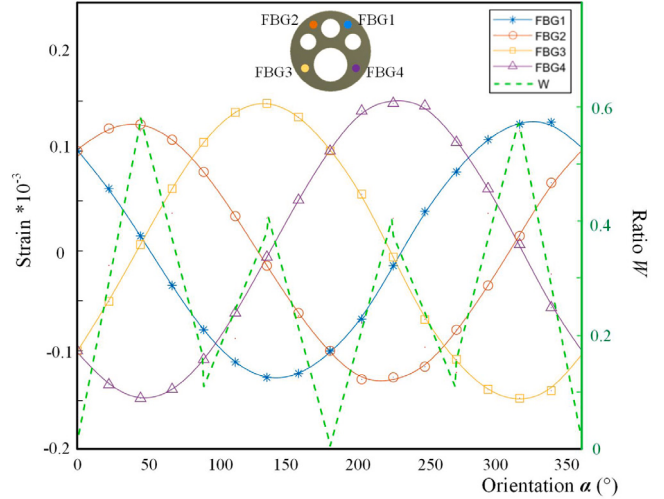


Fig. 7. The relationship between orientation and strain(simulation result).

in a specific orientation, the two fibers closest to that are elongated by tension with a positive slope, while the other two, which are farther away, are shortened by compression with a negative slope. When the magnitude of force F_n is set at 0.5 N, the relation between orientation and strain is shown in **Fig. 7**. It can be seen that the magnitude relationships are consistent with the theory.

3. Experiments and results

3.1. Fabrication and pre-tensioning

The parts required for the Tac-scope sensor fabrication are shown in the upper left of **Fig. 8**. In order to shorten the fabrication cycle and save cost, the rigid part of the sensor is made by resin using additive manufacturing (8200pro material of WeNext Technology Co., Ltd.), and the soft part is made by silicone using mold infusion (White soft silicon material of WeNext Technology Co., Ltd.), with hardness of 30 HA. The parameters of four FBGs are selected as the center wavelength of 1545 nm, grid length of 5 mm (acrylate recoating), bandwidth < 0.4 nm, side-mode rejection ratio > 12 dB, and reflectivity > 50% (Shenzhen Guangchi technology Co., Ltd.). The steps of sensor fabrication and fiber pre-tensioning are shown in **Fig. 8**. In step 1, three layers of parts are aligned and glued. In step 2, four optical fibers from the hole through and pasted to fix one end. This structure is fixed in the pre-tensioning fixture, and will be 100 g weights fixed to the free end of the fiber through the pulley. The fiber is connected to the demodulator and computer to monitor the real-time wavelength shift to ensure that it is a certain value. The stretched end of the fiber is then firmly affixed. Repeat four times to pre-tensioning optical fibers, and the sensor fabrication is complete.

3.2. Calibration

The calibration experiment is designed, and the setup is shown in **Fig. 9**. The system includes the designed Tac-scope sensor, FBG demodulator (M4151-16-25), Taiyo force sensor (DY LY-108 5 N), NI data acquisition card (NI USB-6001), motorized linear stage (NSS120-S450), rotary stage (REG25) and manual linear stage (LGX60-C and LY60LM). By controlling the motorized stage, a continuous force F_n from 0 N to 1.5 N is gradually applied to the sensor, which data and the DY force sensor data are recorded by the demodulator, the software of the computer, and the NI acquisition card, respectively. Each force application and release process are repeated 5 times at the same contact

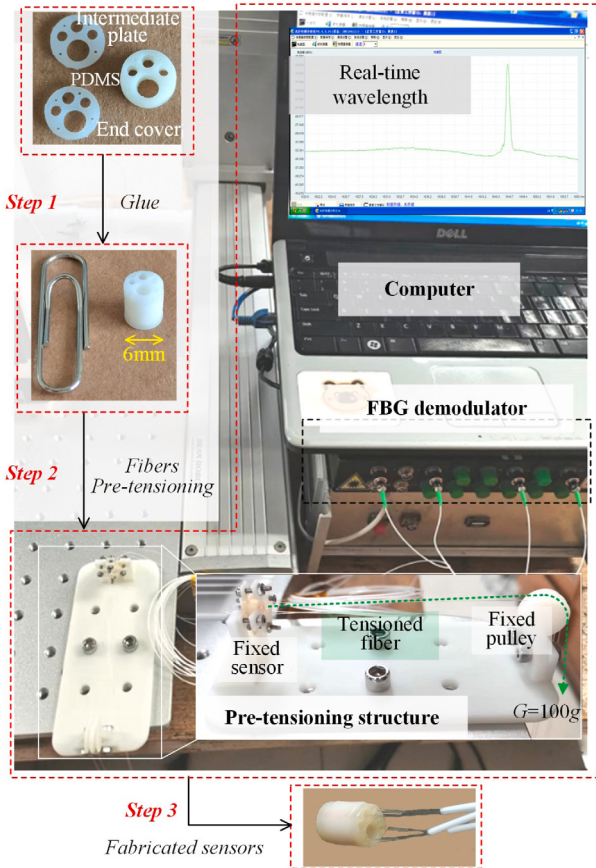


Fig. 8. Sensor fabrication and fibers pre-tensioning.

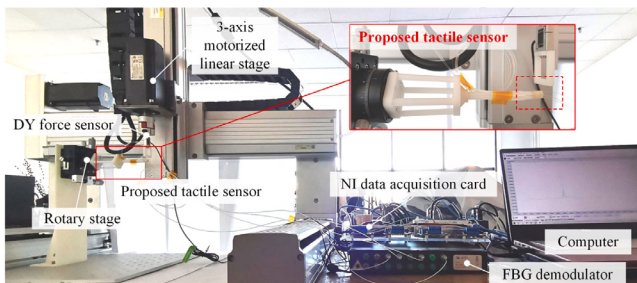


Fig. 9. Setup of sensor calibration.

Table 2
Average repeatability error for each point.

Orientation	0°	22.5°	45°	67.5°	90°	112.5°	135°	157.5°
Error	6.15%	6.12%	6.06%	6.78%	6.66%	5.82%	7.68%	6.27%
Orientation	180°	202.5°	225°	247.5°	270°	292.5°	315°	337.5°
Error	5.73%	6.24%	6.33%	6.75%	6.57%	7.56%	5.94%	6.69%

orientation. Every 22.5° of the sensor periphery is selected as a contact point. The degrees are controlled by the rotary stage.

The experimental results are shown in Fig. 10. It can be seen that the proposed Tac-scope sensor shows a good linear relationship and good repeatability between force and the wavelength shift. The average repeatability error for each test point is listed in Table 2, which shows that the repeatability error of the sensor is 6.46%. The average hysteresis error at different orientations is 6.76%, the average R^2 is 0.991, the root mean square error (RMSE) is 0.0211 nm, the resolution is 8.8 mN, and the sensitivity is 0.693 nm/N. The relationship between

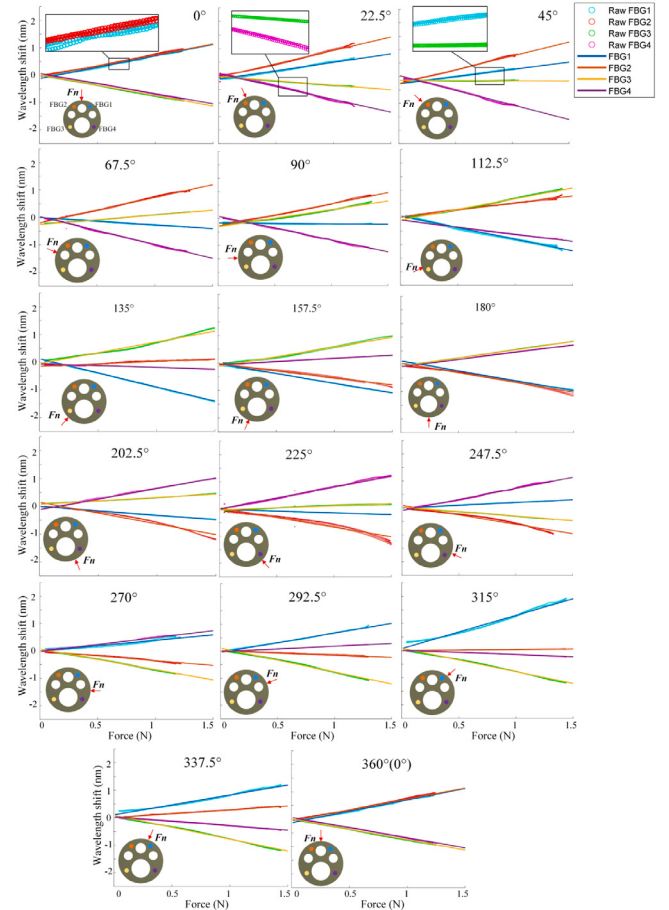


Fig. 10. The relationship between force and wavelength shift (experimental result).

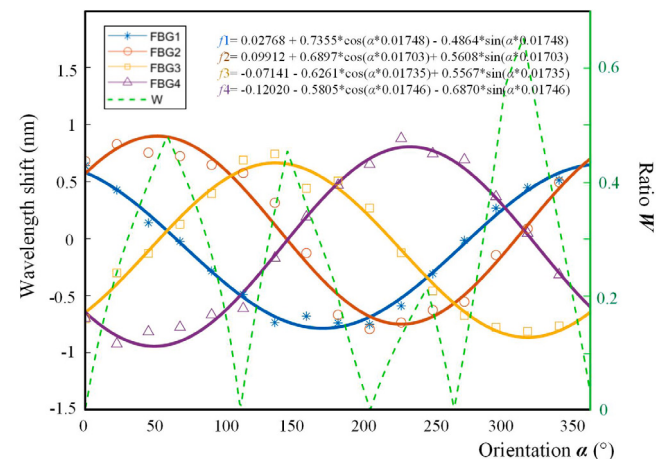


Fig. 11. The relationship between orientation and wavelength shift (experimental result).

the wavelength shifts and orientations when the force is 1 N is shown in Fig. 11. The relationships of FBG1-FBG4 wavelength shifts and orientations are fitted as trigonometric curves f_1-f_4 with R^2 of 0.989, 0.984, 0.989, 0.993, and RMSE of 0.076, 0.093, 0.071, 0.063, respectively. It can be concluded that the experimental results are consistent with the theoretical and simulation results.

W can be fitted as:

$$W = \begin{cases} 0.009159\alpha + 0.02827 & 0^\circ \leq \alpha < 57^\circ \\ -0.01049\alpha + 1.1168 & 57^\circ \leq \alpha < 106^\circ \\ 0.01233\alpha - 1.274 & 106^\circ \leq \alpha < 144^\circ \\ -0.01043\alpha + 2.011 & 144^\circ \leq \alpha < 189^\circ \\ 0.0106\alpha - 1.988 & 189^\circ \leq \alpha < 231^\circ \\ -0.01218\alpha + 3.289 & 231^\circ \leq \alpha < 268^\circ \\ 0.01086\alpha - 2.849 & 268^\circ \leq \alpha < 312^\circ \\ -0.009984\alpha + 3.641 & 312^\circ \leq \alpha < 360^\circ \end{cases} \quad (10)$$

Substitute into Eq. (8):

$$\alpha = \begin{cases} 109.18[(\Delta\lambda_4 - \Delta\lambda_3)(\Delta\lambda_4 - \Delta\lambda_2)^{-1} - 0.02827] & 0^\circ \leq \alpha < 57^\circ \\ -95.33[(\Delta\lambda_4 - \Delta\lambda_1)(\Delta\lambda_4 - \Delta\lambda_2)^{-1} - 1.168] & 57^\circ \leq \alpha < 106^\circ \\ 81.10[(\Delta\lambda_1 - \Delta\lambda_4)(\Delta\lambda_1 - \Delta\lambda_3)^{-1} + 1.274] & 106^\circ \leq \alpha < 144^\circ \\ -95.88[(\Delta\lambda_1 - \Delta\lambda_2)(\Delta\lambda_1 - \Delta\lambda_3)^{-1} - 2.011] & 144^\circ \leq \alpha < 189^\circ \\ 93.90[(\Delta\lambda_2 - \Delta\lambda_1)(\Delta\lambda_2 - \Delta\lambda_4)^{-1} + 1.988] & 189^\circ \leq \alpha < 231^\circ \\ -82.10[(\Delta\lambda_2 - \Delta\lambda_3)(\Delta\lambda_2 - \Delta\lambda_4)^{-1} - 3.289] & 231^\circ \leq \alpha < 268^\circ \\ 92.08[(\Delta\lambda_3 - \Delta\lambda_2)(\Delta\lambda_3 - \Delta\lambda_1)^{-1} + 2.849] & 268^\circ \leq \alpha < 312^\circ \\ -100.16[(\Delta\lambda_3 - \Delta\lambda_4)(\Delta\lambda_3 - \Delta\lambda_1)^{-1} - 3.641] & 312^\circ \leq \alpha < 360^\circ \end{cases} \quad (11)$$

The interval of contact orientation can be obtained from the relationship between the wavelength shifts of calibration curve (Fig. 11).

3.3. Compensation of human dynamic parameter

The human body is a complex system, body temperature has differences, and it will change during the operation. The humidity of the human airways is in the range of 80%–100% [35], with specific values varying according to individual differences. In addition, airway surface liquid pH in vivo is around 7.0, 6.6 ± 0.1 in upper airways, 7.1 ± 0.1 in lower airways [36], which is a neutral environment. For the proposed sensor, fibers are encapsulated inside to prevent it from being exposed to environments in the human body. And the encapsulation materials such as epoxy resin, polytetrafluoroethylene (PTFE) can resist the effect of humidity and PH on the sensor. However, the sensor itself is sensitive to temperature, so, it is necessary to compensate the temperature in order to avoid the detection error.

As shown in Fig. 12(a), the sensor is placed in the electrothermal constant-temperature blast drying oven (DHG-9145 A, resolution 0.1°C), heated from room temperature to 30°C , and kept at a constant temperature for about 1 h every 2°C increases. The wavelength shifts of FBGs are recorded as shown in Fig. 12(b). Taking the average value of the wavelength shift of each FBG in the temperature stable interval in each time period. The temperature and wavelength shift can be fitted as a linear relationship, as shown in Fig. 12(c).

According to the fitting results, the temperature sensitive coefficients of FBGs are $13.41 \text{ pm}/^\circ\text{C}$, $15.29 \text{ pm}/^\circ\text{C}$, $13.19 \text{ pm}/^\circ\text{C}$, $13.67 \text{ pm}/^\circ\text{C}$ and $9.817 \text{ pm}/^\circ\text{C}$, respectively. R^2 are 0.9991 , 0.9991 , 0.9992 and 0.9987 , respectively. The temperature proportional coefficients are $t_1 = 1.366$, $t_2 = 1.5575$, $t_3 = 1.3436$ and $t_4 = 1.3925$, respectively. According to the principle of temperature compensation in Section 2.3, the wavelength shifts after compensation are plotted as shown in Fig. 12(b). The average temperature compensation errors are 5.49%, 4.32%, 1.02% and 3.13% respectively, and the average variance is 6.03 pm.

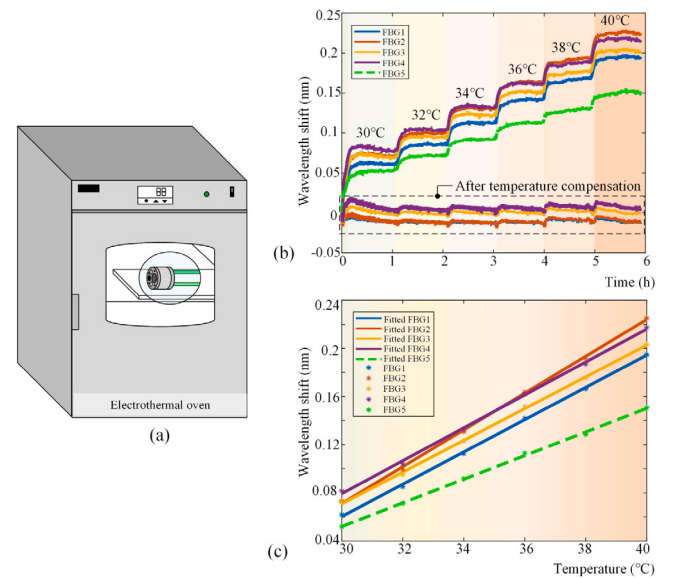


Fig. 12. Temperature compensation of the sensor. (a) Setup (b) Real-time wavelength shift of FBGs in the process of heating and insulation (c) Relationship between wavelength shifts and temperature.

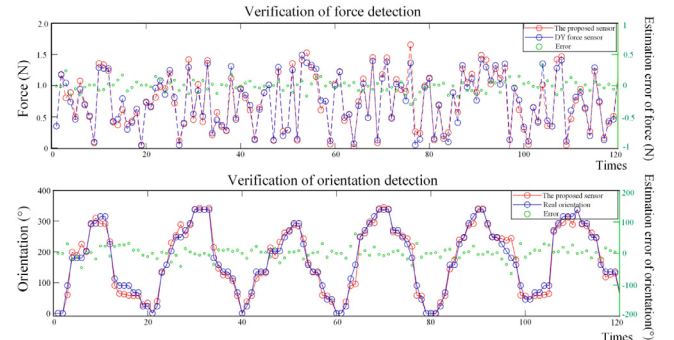


Fig. 13. Test results under the random magnitude force applied at random orientation.

3.4. Verification

The Tac-scope sensor verification setup is the same as that shown in Fig. 9. Ten random contact orientations are selected at the periphery of the sensor by the rotary stage, and a random force from 0 N to 1.5 N is applied by the motorized linear stage. A total of twelve groups of random tests are conducted, and the results are shown in Fig. 13. In order to facilitate analysis, the test data of each group are sorted according to the real orientations. It can be seen that the detected force value and orientation obtained by the proposed sensor are in good agreement with the real values. The average error of force detection is 0.067 N and of orientation detection is 3.57% (i.e., 0.67 mm). In addition, the response time of the force and orientation estimation program is about 36 ms.

3.5. Test on bronchial model

In order to verify the capability of the Tac-scope, a flexible structure (continuum arm) same as the bending section of the endoscope is fabricated, as shown in Fig. 14. A driving rope is used to give the continuum arm one bending degree of freedom (DOF). A metal hose with cladding is attached to it. A four-stage transparent bronchial model is used as the object of endoscopic inspection. The Tac-scope

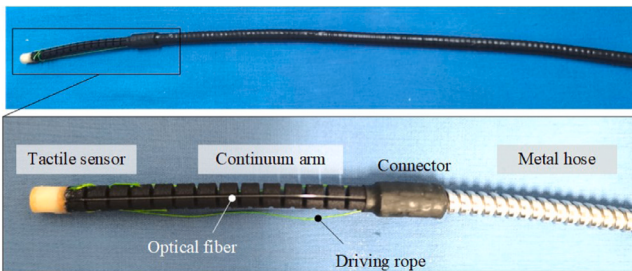


Fig. 14. The endoscope integrated with the tactile sensor.

is manually controlled to reach three selected target positions, and the detected contact force value and orientation are recorded during the process, as shown in Fig. 15.

The results show that the Tac-scope can identify the magnitude and orientation of force. In the process, the endoscope is likely to have stronger contact at P1, P2, and the destination, as shown in Fig. 15 (a2)(a3)(b2)(b3)(c2)(c3). In order to visualize the contact orientation intuitively, the data is corresponded to polar coordinates. As shown, the orientations are mainly concentrated on the lower right side of the Tac-scope. Since it has only one DOF for bending, the contact orientation is mostly on the outside of the bend. Fig. 15 (a2)(b2)(c2) show the test results under vision only, and Fig. 15 (a3)(b3)(c3) show the test results under vision and real-time tactile feedback prompts (the interface and details are shown in Section 3.7). It can be seen that the contact force of the latter is less than that of the former, with an average reduction of about 60%, and the time is also shortened, with an average reduction of about 30%.

In order to provide more information about the robustness of Tac-scope (in the temporal dimension), a follow-up test is conducted 5 months after the initial assessment. The results are presented in Fig. 15(a4)(b4)(c4). It can be observed that the sensor continue to exhibit stable detection, with no indications of sensitivity or other properties change. However, there are random effects such as jitter in the manual operation of each test, which leads to differences in the testing process (inconsistent length of time or contact at each location). Nevertheless, after 5 months, there is no discernible change in the sensor's force detection ability or effect.

3.6. Test on *in vitro* porcine lungs

To ascertain the efficacy of the Tac-scope in detecting bronchial tissue, fresh *in vitro* porcine lungs are used. The lungs lacked the main trachea, with the left and right main bronchi remaining. Therefore, endoscope insertion experiments are conducted on the left and right lungs, respectively, as illustrated in Fig. 16(a1) (b1). The contact force, orientation and images during the process are recorded and shown in Fig. 16, demonstrating that the Tac-scope is capable for soft bronchi detecting. The contact force in the left and right lungs are at a low level, which is comparable to that in the bronchial model. The centralized contact orientation may be attributed to the limited DOF of the endoscope, and the lack of training in controlling the endoscope steering in the lungs.

3.7. Tactile-visual real-time feedback

In order to realize intuitive real-time feedback, the endoscopic image is combined with tactile information. In order to avoid cognitive fatigue, the color circle [37] is used for real-time tactile feedback in the endoscopic visual field interface, as shown in Fig. 17. The contact orientation of the Tac-scope corresponds to the color circles around the visual field. Dark green, bright green, yellow, and red corresponding to no contact, $0 < \text{contact force} < 0.25 \text{ N}$, $0.25 \text{ N} < \text{contact force} < 0.5$

Table 3
Comparison with other force sensors.

Sensors	Error	Sensitivity	Resolution
[16]	16%	–	1 kPa
[23]	5.3%	0.47 nm/N	23.12 mN
[25]	5.4%	1.30 nm/N	1.19 mN
This paper	4.4%	0.69 nm/N	8.8 mN

N, and contact force $> 0.5 \text{ N}$, respectively. Total feedback time of the visual-tactile system is less than 120 ms, allowing the surgeon to adapt and perform the procedure safely and efficiently [38]. This approach intuitively feeds real-time tactile and visual information back to the operator, realizing timely endoscopic control and avoiding tracheal injury.

4. Discussion and conclusion

This article proposes the Tac-scope, an endoscope integrated with an embedded soft tactile sensor that enables contact force sensing and real-time tactile feedback. The Tac-scope retains the functions of a regular endoscope while also allowing for soft contact with the lumen wall. The detection ability of the Tac-scope sensor has been verified through theoretical analysis, simulated analysis, and experiments. The force detection linearity is 0.991, with a repeatability error of 6.46%, a resolution of 8.8 mN, a sensitivity of 0.693 nm/N and an average error of 0.067 N (4.4%). The average error of orientation detection is 3.57% (i.e. 0.67 mm). The comparison of sensors' parameters is shown in Table 3. It can be seen that the error of proposed sensor is less than that of others in the list, and the sensitivity and resolution are also at a superior level. Tac-scope has better overall performance. The flexible Tac-scope's ability to operate in complex luminal environment is demonstrated through testing on a bronchial model. Real-time tactile feedback capability is achieved through tactile-visual fusion feedback testing on the model. The combination of haptics and endoscopic visual field provides intuitive feedback of intraoperative information, enhancing surgical safety and efficiency. The contact force is reduced by 60%, and the operation time is shortened by 30%. Tac-scope's compact size enables its use in other NOTES, including transurethral, vaginal endoscopic, and gastrointestinal endoscopic surgeries, with potential for application and promotion.

Nevertheless, the current study is still limited. The tumor hardness information has not been provided, which can help surgeons make comprehensive diagnosis. In future research, the precise location of subcutaneous tumors intraoperatively through hardness palpation by using biopsy forceps will be conducted. Then, due to the limitation of experimental conditions, the first generation of sensor is made at a low cost, and only performance tests are done without strict encapsulation and the use of sterilizable materials. In future research, stainless steel will be used instead of resin for sterilizability, and PTFE will be used for overall encapsulation. The material optimized and encapsulated Tac-scope can be easily calibrated for normal use since the principle of detection has not changed. The Tac-scope has been tested more than 900 times during the experimental period, and the longest interval between tests is more than 1 year. During the period of water immersion, rinsing, the sensor can still be used and there is no appreciable change in the parameters. If PTFE encapsulation is used, the longevity can be much longer. In addition, the FBG demodulator is not small enough for integration in surgical robot. 4 channels will be used to reduce the size by a factor of 3–4 instead of 16 channels. Furthermore, the digital twin of surgical robot based on multi-mode sensing will be centered, integrating endoscopic image and end force feedback, shape sensing and body force distribution, and human–robot interaction.

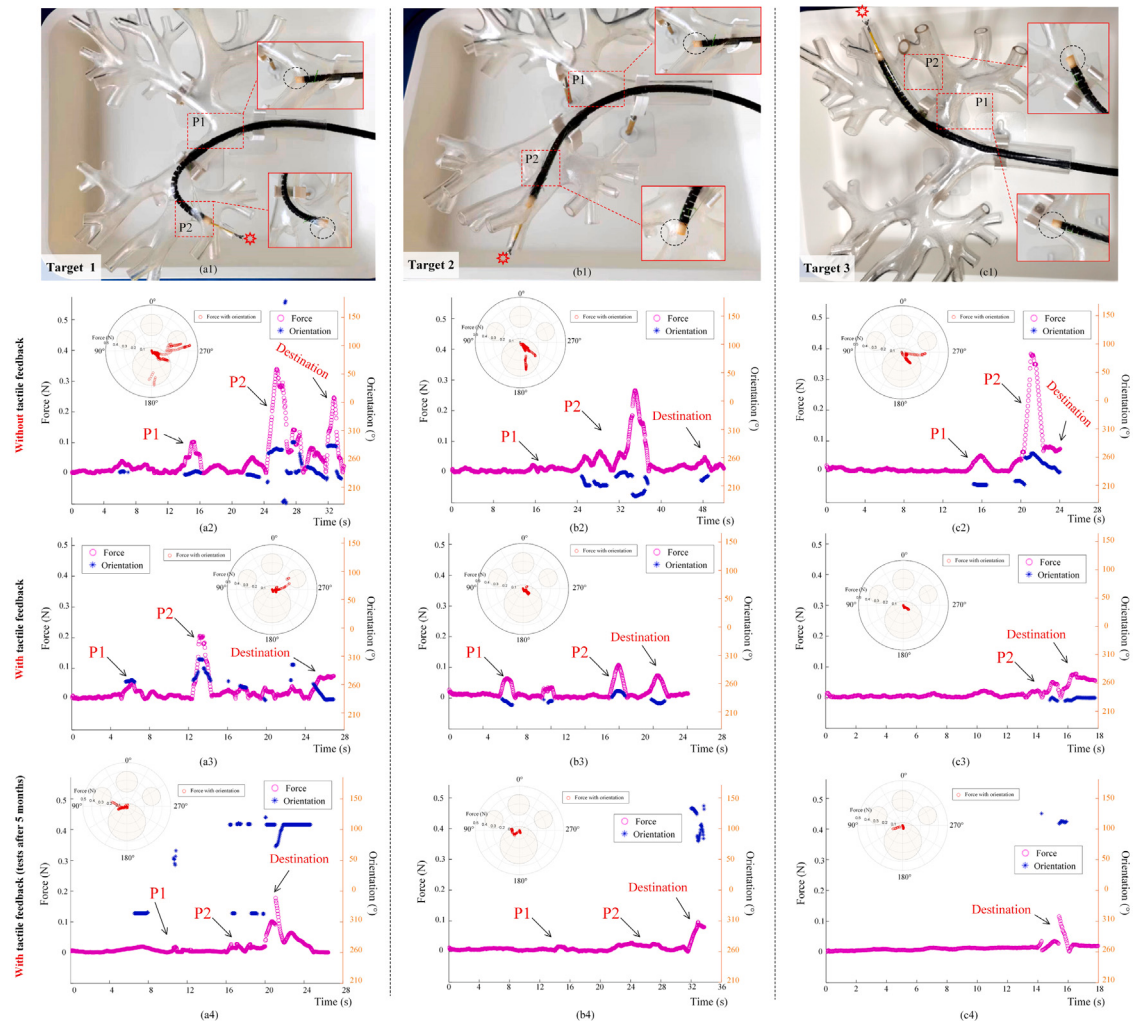


Fig. 15. Tests on bronchial model. (a1) Target 1 (a2) Test result of target 1 without tactile feedback (a3) Test result of target 1 with tactile feedback (a4) Test result of target 1 with tactile feedback after 5 months (b1) Target 2 (b2) Test result of target 2 without tactile feedback (b3) Test result of target 3 with tactile feedback (b4) Test result of target 2 with tactile feedback after 5 months (c1) Target 3 (c2) Test result of target 3 without tactile feedback (c3) Test result of target 3 with tactile feedback (c4) Test result of target 3 with tactile feedback after 5 months.

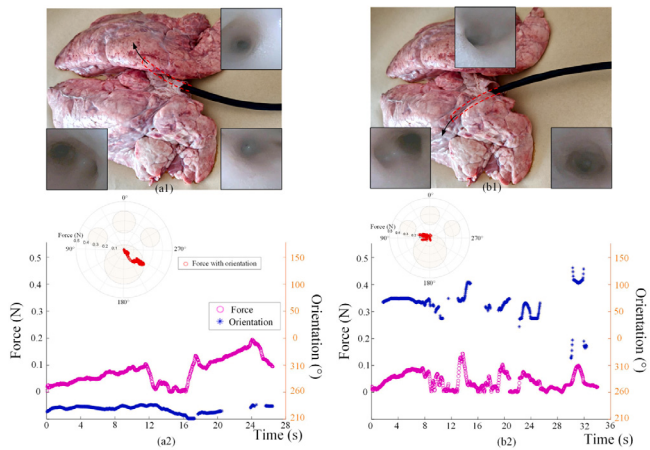


Fig. 16. Test on in vitro porcine lungs. (a1) Left lung (a2) Test result of the left lung (b1) Right lung (b2) Test result of the right lung.

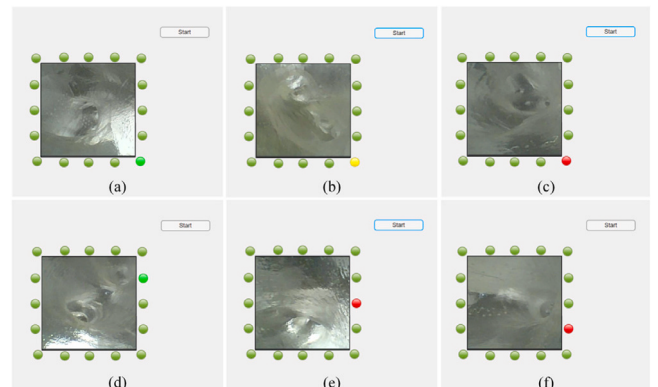


Fig. 17. Tactile-visual real-time feedback interface. (a)–(f) one of the contact conditions.

CRediT authorship contribution statement

Yingxuan Zhang: Writing – review & editing, Writing – original draft, Visualization, Validation, Software, Methodology, Investigation, Data curation, Conceptualization. **Qi Jiang:** Writing – review & editing, Supervision, Project administration, Funding acquisition. **Feiwen Wang:** Writing – review & editing, Software, Resources, Methodology, Data curation. **Jie Wang:** Writing – review & editing. **Maosheng Ye:** Writing – review & editing. **Dongxuan Li:** Writing – review & editing.

Declaration of competing interest

The authors declare that they have no known competing financial interests or personal relationships that could have appeared to influence the work reported in this paper.

Data availability

The data that has been used is confidential.

Acknowledgments

This work was partly supported by the National Natural Science Foundation of China [grant number 61973194]; and the National Key Research and Development Program of China [grant number 2017YFB1302 102].

References

- [1] Y. Juo, A. Abiri, J. Pensa, Center for advanced surgical and interventional technology multimodal haptic feedback for robotic surgery, in: *Handbook of Robotic and Image-Guided Surgery*, 2020, pp. 285–301.
- [2] A.H. Hadi Hosseiniabadi, S.E. Salcudean, Force sensing in robot-assisted keyhole endoscopy: A systematic survey, *Int. J. Robot. Res.* 41 (2) (2021) 136–162, <http://dx.doi.org/10.1177/02783649211052067>.
- [3] C.J. Payne, H. Rafii-Tari, G. Yang, A force feedback system for endovascular catheterisation, in: *The 2012 IEEE/RSJ International Conference on Intelligent Robots and Systems, IROS, Vilamoura, Algarve Portugal*, 2013, pp. 1298–1304.
- [4] O. Hung, M. Murphy, *Manage the Difficult and Failed Airway*, first ed., McGraw-Hill Medical Press, New York, USA, 2008.
- [5] X.T. Ha, et al., Contact localization of continuum and flexible robot using data-driven approach, *IEEE Robot. Autom. Lett.* 7 (3) (2022) 6910–6917, <http://dx.doi.org/10.1109/LRA.2022.3176723>.
- [6] C. Zhang, S. Guo, B. Gao, F. Jia, The beam theory-based collision force detection of the catheter operating system, in: *2016 IEEE International Conference on Mechatronics and Automation, Harbin, China*, 2016, pp. 701–706.
- [7] P. Shi, S. Guo, L. Zhang, et al., Design and evaluation of a haptic robot-assisted catheter operating system with collision protection function, *IEEE Sens. J.* 21 (18) (2021) 20807–20816, <http://dx.doi.org/10.1109/JSEN.2021.3095187>.
- [8] A.L. Trejos, A.C. Lyle, A. Escoto, M.D. Naish, R.V. Patel, Force/position-based modular system for minimally invasive surgery, in: *2010 IEEE International Conference on Robotics and Automation, Anchorage, AK, USA*, 2010, pp. 3660–3665, <http://dx.doi.org/10.1109/ROBOT.2010.5509964>.
- [9] B. Guan, X. Liu, Z. Ma, et al., Safety motion control and end force estimation based on angle information in robotic flexible endoscopy, *Intell. Robot. Appl.* (2022) 396–408.
- [10] Z. Wang, G. Liu, S. Qian, et al., Tracking control with external force self-sensing ability based on position/force estimators and non-linear hysteresis compensation for a backdrivable cable-pulley-driven surgical robotic manipulator, *Mech. Mach. Theory* 183 (2023) http://dx.doi.org/10.1007/978-3-031-13835-5_36.
- [11] W. Lai, L. Cao, R.X. Tan, et al., An integrated sensor-model approach for haptic feedback of flexible endoscopic robots, *Ann. Biomed. Eng.* 48 (1) (2020) 342–356, <http://dx.doi.org/10.1007/s10439-019-02352-8>.
- [12] I.Sur sić, A. Zam, P.C. Cattin, et al., Enabling minimal invasive palpation in flexible robotic endoscopes, *New Trends Med. Serv. Robot.* (2019) 70–77, http://dx.doi.org/10.1007/978-3-030-00329-6_9.
- [13] T. Nagatomo, N. Miki, A flexible tactile sensor to detect stiffness distribution without measuring displacement, in: *International Conference on Solid-State Sensors, Actuators and Microsystems & Eurosensors XXXIII, TRANSDUCERS & EUROSENSORS XXXIII, Berlin, Germany*, 2019, pp. 551–555, <http://dx.doi.org/10.1109/transducers.2019.8808756>.
- [14] M.O. Shaikh, C.-M. Lin, D.-H. Lee, et al., Portable pen-like device with miniaturized tactile sensor for quantitative tissue palpation in oral cancer screening, *IEEE Sens. J.* 20 (17) (2020) 9610–9617, <http://dx.doi.org/10.1109/JSEN.2020.2992767>.
- [15] Y. Zhang, X. Wei, W. Yue, et al., A dual-mode tactile hardness sensor for intraoperative tumor detection and tactile imaging in robot-assisted minimally invasive surgery, *Smart Mater. Struct.* 30 (8) (2021) <http://dx.doi.org/10.1088/1361-665X/ac112b>.
- [16] A.S. Naidu, R.V. Patel, M.D. Naish, Low-cost disposable tactile sensors for palpation in minimally invasive surgery, *IEEE-ASME Trans. Mechatronics* 22 (1) (2017) 127–137, <http://dx.doi.org/10.1109/TMECH.2016.2623743>.
- [17] U. Kim, Y.B. Kim, D.-Y. Seok, et al., A surgical palpation probe with 6-axis force/torque sensing capability for minimally invasive surgery, *IEEE Trans. Ind. Electron.* 65 (3) (2018) 2755–2765, <http://dx.doi.org/10.1109/TIE.2017.2739681>.
- [18] X. Jin, S. Guo, J. Guo, et al., Total force analysis and safety enhancing for operating both guidewire and catheter in endovascular surgery, *IEEE Sens. J.* 21 (20) (2021) 22499–22509, <http://dx.doi.org/10.1109/JSEN.2021.3107188>.
- [19] R. Ankur, R.H. Baheti, S. Pai, J. Gomez, Y. Millo, J.P. Desai, Real-time fiber-optic intubation simulator with force feedback, *IEEE/ASME Trans. Mechatronics* 17 (1) (2012) 98–106, <http://dx.doi.org/10.1109/TMECH.2010.2090666>.
- [20] X. Guo, Y. Li, et al., Bamboo-inspired, environmental friendly PDMS/Plant fiber composites-based capacitive flexible pressure sensors by Origami for Human-Machine interaction, *ACS Sustain. Chem. Eng.* 12 (12) (2024) 4835–4845, <http://dx.doi.org/10.1021/acssuschemeng.3c06949>.
- [21] X. Guo, W. Hong, et al., Bioinspired dual-mode stretchable strain sensor based on magnetic nanocomposites for strain/magnetic discrimination, *Small* 19 (2023) 2205316, <http://dx.doi.org/10.1002/smll.202205316>.
- [22] X. Guo, T. Zhang, et al., Tactile corpuscle-inspired piezoresistive sensors based on (3-aminopropyl) triethoxysilane-enhanced CNPs/carboxylated MWNTs/cellulosic fiber composites for textile electronics, *J. Colloid Interface Sci.* 660 (2024) 203–214, <http://dx.doi.org/10.1016/j.jcis.2024.01.059>.
- [23] T. Li, C. Shi, H. Ren, Three-dimensional catheter distal force sensing for cardiac ablation based on fiber Bragg grating, *IEEE/ASME Trans. Mechatronics* 23 (5) (2018) 2316–2327, <http://dx.doi.org/10.1109/TMECH.2018.2867472>.
- [24] T. Zhang, B. Chen, S. Zuo, A novel 3-DOF force sensing microneedle with integrated fiber Bragg grating for microsurgery, *IEEE Trans. Ind. Electron.* 69 (1) (2022) 940–949, <http://dx.doi.org/10.1109/TIE.2021.3055173>.
- [25] W. Lai, L. Cao, J. Liu, et al., Three-axial force sensor based on fiber Bragg gratings for surgical robots, *IEEE/ASME Trans. Mechatronics* 27 (2) (2022) 777–789, <http://dx.doi.org/10.1109/TMECH.2021.3071437>.
- [26] C. Du, D. Wei, H. Wang, et al., Development of the X-Perce—A universal FBG-based force sensing kit for laparoscopic surgical robot, *IEEE Trans. Med. Robot. Bionics* 4 (1) (2022) 183–193, <http://dx.doi.org/10.1109/TMRB.2022.3145618>.
- [27] Z. Ping, T. Zhang, L. Gong, et al., Miniature flexible instrument with fibre Bragg grating-based triaxial force sensing for intraoperative gastric endomicroscopy, *Ann. Biomed. Eng.* 49 (9) (2021) 2323–2336, <http://dx.doi.org/10.1007/s10439-021-02781-4>.
- [28] F. Masaki, F. King, T. Kato, H. Tsukada, Y. Colson, N. Hata, Technical validation of multi-section robotic bronchoscope with first person view control for transbronchial biopsies of peripheral lung, *IEEE Trans. Biomed. Eng.* 68 (2021) 3534–3542, <http://dx.doi.org/10.1109/TBME.2021.3077356>.
- [29] X. Jin, et al., Total force analysis and safety enhancing for operating both guidewire and catheter in endovascular surgery, *IEEE Sens. J.* 21 (20) (2021) 22499–22509, <http://dx.doi.org/10.1109/JSEN.2021.3107188>.
- [30] B. Winkeljann, P.-M.A. Leipold, O. Lieleg, Macromolecular coatings enhance the tribological performance of polymer-based lubricants, *Adv. Mater. Interfaces* 6 (16) (2019) 1900366, <http://dx.doi.org/10.1002/admi.201900366>.
- [31] Z. Zhou, J. Ou, Techniques of temperature compensation for FBG strain sensors used in long-term structural monitoring, in: Paper Presented At Fundamental Problems of Optoelectronics and Microelectronics II, 2005, <http://dx.doi.org/10.1117/12.634047>.
- [32] A.D. Kersey, M.A. Davis, H.J. Patrick, M. LeBlanc, K.P. Koo, C.G. Askins, M.A. Putnam, E.J., Friebele fiber grating sensors, *Lightwave Technol.* 15 (8) (1997) 1442–1463.
- [33] Y. Zhang, Q. Jiang, F. Wang, J. Wang, FBG tactile sensor integrated on bronchoscope for force and contact position sensing, in: *Intelligent Robotics and Applications, ICIRA 2023, Hangzhou, China*, 14271, 2023, http://dx.doi.org/10.1007/978-981-99-6495-6_4.
- [34] Y. Zhang, F. Ju, X. Wei, et al., A piezoelectric tactile sensor for tissue stiffness detection with arbitrary contact angle, *Sensors* 20 (22) (2020) <http://dx.doi.org/10.3390/s20226607>.
- [35] Hou Dapeng, Jiang Zhi, Impact of ambient temperature on the humidification of respiratory tract during mechanical ventilation, *Chinese J. Crit. Care Med.* 28 (12) (2008) 1108–1110.
- [36] D. McShane, J.C. Davies, M.G. Davies, A. Bush, D.M. Geddes, E.W.F.W. Alton, Airway surface pH in subjects with cystic fibrosis, *Eur. Respir. J.* 21 (2003) 37–42, <http://dx.doi.org/10.1183/09031936.03.00027603>.
- [37] A.I. Aviles-Rivero, S.M. Alsaleh, J. Philbeck, et al., Sensory substitution for force Feedback recovery, *ACM Trans. Appl. Percept.* 15 (3) (2018) 1–19, <http://dx.doi.org/10.1145/3176642>.
- [38] X. Zhou, J. Wang, et al., Ultra-remote robot-assisted laparoscopic surgery for varicocele through 5G network: Report of two cases and review of the literature, *Natl. J. Androl.* 28 (8) (2022) 696–701.